Local Structural Coherence and Interfacial Charge Transfer in Cu_2S/MoS_2 Heterostructure

Ankita Kumari,[1] S. Avery Vigil,[2] Konstantina G. Mason,[3] Saurabh Sivakumar,[4] Ahmed H. Biby,[5] Pranay Ninawe,[3] Charles B. Musgrave,[6,7,*] Ambarish R. Kulkarni,[4,†] Ivan A. Moreno-Hernandez,[2,‡] and Jesús M. Velázquez[1,3,4,§]

[1] *Agricultural and Environmental Chemistry Graduate Group, University of California, Davis, One Shields Avenue, Davis, California 95616, USA*

[2] *Department of Chemistry, Duke University, Durham, North Carolina, 27708, USA*

[3] *Department of Chemistry, University of California, Davis, One Shields Avenue, Davis, California 95616, USA*

[4] *Department of Chemical Engineering, University of California, Davis, One Shields Avenue, Davis, California 95616, USA*

[5] *Materials Science and Engineering Program, University of Colorado Boulder, Boulder, Colorado 80309, USA*

[6] *Department of Chemical Engineering, University of Utah, Salt Lake City, Utah 84112, USA*

[7] *Department of Materials Science and Engineering, University of Utah, Salt Lake City, Utah 84112, USA*

(Received 5 March 2026; revised 24 April 2026; accepted 12 May 2026; published 9 June 2026)

Precise control over electronic coupling at nanoscale interfaces is critical for designing materials with tunable charge-transfer behavior and catalytic function. Heterostructures with locally coherent interfaces provide a platform for interrogating interfacial charge redistribution in coupled material systems. Here, we report Cu_2S/MoS_2 heterostructures exhibiting nanoscale crystallographic alignment, which are synthesized through a rapid thermal transformation pathway. We employed electrochemical reduction reactions to probe interfacial charge transfer, revealing shifts in product distribution attributable to modified interfacial energetics, even in the absence of optimized catalytic performance. The observed formate Faradaic efficiency suggests that interfacial electronic modulation in the heterostructure shifts product selectivity towards formate, highlighting how interface-driven electronic modulation can direct reaction pathways and influence product selectivity. Optimizing catalyst loading, architecture, and reactor configuration will be critical for future improvement. Structural and compositional integrity were confirmed through powder x-ray diffraction, x-ray photoelectron spectroscopy, and high-resolution transmission electron microscopy. Electron transfer between Cu_2S and MoS_2 domains was further evaluated by electrochemical impedance spectroscopy, while selected-area electron diffraction revealed local crystallographic alignment consistent with a local epitaxial relationship at the Cu_2S/MoS_2 heterointerface. To illustrate the broader applicability of this approach, a ZnS/MoS_2 heterostructure was also synthesized using the same microwave strategy, confirming the generalizability of interfacial engineering principles across metal sulfide-MoS_2 systems. Collectively, these findings demonstrate that controlled local epitaxial alignment serves as an effective design principle for tuning interfacial energetics and catalytic reactivity in complex heterostructure materials.

DOI: 10.1103/84s6-812t

I. INTRODUCTION

The synthesis of two-dimensional heterostructures comprising nanosheets and nanowires has attracted interest from both fundamental and application perspectives. The rational assembly of heterostructures made from diverse materials enables new properties to emerge through interfacial synergy, offering a pathway to overcome individual material limitations [1]. Furthermore, in electrochemical reactions, heterostructure materials offer several benefits, including interfacial electron

*Contact author: charles.musgrave@utah.edu
†Contact author: arkulkarni@ucdavis.edu
‡Contact author: ivan.moreno-hernandez@duke.edu
§Contact author: jevelazquez@ucdavis.edu

redistribution, which modifies active sites and accelerates reaction kinetics, as well as surface reconstruction, charge transfer, and delocalization [2–6].

The synthesis of hierarchical structures can be realized through rationally designed synthetic strategies that overcome diffusion-limited growth, enabling the formation of structurally well-defined heterostructures [7–10]. Despite considerable efforts, achieving reproducible nanoheterostructures with locally coherent and crystallographically aligned interfaces remains a substantial challenge [11]. Moreover, precise control over morphology and dimensionality is essential, as the catalytic behavior of nanostructured materials is strongly influenced by the nature and orientation of their exposed crystal facets [12]. Conventional thermal synthesis methods, such as furnace annealing or hydrothermal processing, often suffer from long reaction times, nonuniform heating, and limited control over nucleation rates. These conditions can result in irregular morphologies and poor interfacial contact, which compromise charge transfer and catalytic performance. In contrast, microwave irradiation delivers rapid volumetric heating and localized superheating, which promote uniform nucleation, reduced diffusion barriers, and improved control over nanoscale morphology. These conditions can promote localized crystallographic alignment and interfacial coherence, providing a platform for probing how the interfacial structure influences charge redistribution [13–15].

Recently, transition-metal dichalcogenides, particularly MoS_2, have emerged as promising candidates for investigating structural modulations induced by forming heterostructures, owing to their unique layered architecture; cost-effectiveness; and inherent advantages, such as a high surface-to-volume ratio, abundantly exposed surface atoms, metal-sulfur covalent bonds, and a π-conjugated structure that facilitates faster electron diffusion [16–19]. Structurally, MoS_2 consists of layers of molybdenum (Mo) atoms arranged in a hexagonal lattice, alternating with two hexagonally arranged layers of sulfur (S) atoms. These S-Mo-S layers are covalently bonded, layered, and held together by weak van der Waals forces. However, $2H$-MoS_2 faces two primary challenges: (i) its desirable catalytic activity is mainly localized at the edge sites, and (ii) its inherent semiconducting nature limits electron transfer, thereby necessitating strategic structural modifications [20–26].

Recent efforts have focused on transition-metal sulfide heterostructures as promising electrocatalysts for CO_2 reduction, leveraging their mixed-valence states, abundant defect sites, and sustainability [2,27,28]. Moreover, these systems exhibit intrinsically high charge conductivity, which is further enhanced by a tunable band gap influenced by the occupancy of metal d orbitals [29,30]. Within this class of materials, copper-based systems are of particular interest for driving multielectron CO_2 reduction, yet monometallic Cu surfaces often exhibit limited activity and poor selectivity [31,32]. To mitigate these drawbacks, structural engineering approaches, including targeted doping, morphology and size control, heterostructure formation, and defect manipulation, have been pursued to modulate surface energetics and guide reaction pathways [20–22,26]. Sulfide-derived Cu frameworks have been demonstrated to tune the relative stabilization of CO_2 reaction intermediates, enabling improved selectivity towards CO, formate, and even C_{2+} products. In addition, transition-metal sulfide heterostructures often exhibit improved structural robustness over a broad pH window, preserving catalytically active surface motifs during extended electrolysis. Such interface-stabilized structures are particularly attractive for carbon capture and utilization, where sustained activity, selectivity control, and long-term operational stability are essential [33–35].

In this context, Cu_2S/MoS_2 heterostructures offer a compelling platform by combining the complementary interfacial and electronic properties of both materials. Despite these advantages, most synthetic approaches provide limited control over interface quality and nanoscale morphology. Recent advances have begun to address these challenges. For instance, Li *et al*. synthesized $MoS_2@C@Cu_2S$ heterostructures via a template-assisted method, producing hollow nanocubes with a high Zn^{2+} storage capacity [36]. Wang *et al*. demonstrated improved hydrogen evolution reaction activity in alkaline media for nitrogen-doped Cu_2S/MoS_2 nanorods. These heterojunction nanorod arrays were synthesized directly on copper foam substrates via a facile hydrothermal method [37]. Recent work by Miller *et al*. demonstrates that chalcogenide frameworks are promising materials for integrated CO_2 utilization and storage, where controlled stabilization of reduced intermediates enables the selective formation of value-added carbon products such as carbonates and oxalates [30]. Other work by Zhao *et al*. demonstrated a Cu_2WS_4/MoS_2 heterostructure composed of multiple metal sulfides constructed via one-pot transformation strategies wherein precursor phases undergo *in situ* conversion into coupled domains [38]. While numerous MoS_2-based heterostructures have been reported, discussions surrounding the influence of synthetic methods on morphological and dimensional control remain limited.

Building on these insights, we report a microwave-assisted synthesis strategy that enables precise control over the morphology and dimensionality of Cu_2S/MoS_2 nanoheterostructures, yielding either sheetlike or tubelike architectures, depending on the reaction conditions. We hypothesize that local epitaxial alignment induced by rapid microwave heating enhances interfacial charge transfer and catalysis by promoting coherent bonding across the Cu_2S/MoS_2 interface and modifying local electronic structures. In addition to Cu_2S/MoS_2, the rational design of other metal sulfide-MoS_2 heterostructures could offer

further insights into how synthetic conditions and interfacial chemistry dictate morphology and catalytic behavior. Demonstrating such generalizability is crucial for validating the broader utility of the microwave-assisted synthesis platform. To this end, we extend our method to the synthesis of ZnS/MoS_2 heterostructures, using a similar precursor transformation pathway under controlled microwave conditions. This comparison allows us to explore structural coherence and phase integration in different systems, reinforcing the modularity of our approach.

The resulting heterostructures were systematically evaluated using powder x-ray diffraction (PXRD), x-ray photoelectron spectroscopy (XPS), high-resolution transmission electron microscopy (HRTEM), and selected-area electron diffraction (SAED), all of which confirmed phase-pure Cu_2S/MoS_2 assemblies with epitaxially integrated Cu_2S domains within the MoS_2 sheets. Morphological analyses by scanning electron microscopy (SEM) and HRTEM further revealed highly ordered nanosheet and nanotube architectures, underscoring the efficacy of the microwave-assisted approach for directing structural coherence and dimensional control. Beyond this specific system, the material design strategy demonstrated is generalizable to other heterostructured frameworks, establishing design principles that can guide active-site modulation and interfacial engineering across a broad range of catalytic materials. Our findings suggest that epitaxial interface engineering can tune activity and selectivity in electrochemical reduction reactions. These insights provide a foundation for advancing the rational design of functional interfaces that can accelerate progress in the broader field of electrocatalysis and small-molecule conversion.

II. EXPERIMENTAL SECTION

The synthesis of Cu_2S/MoS_2 nanoheterostructures involves a multistep pathway including: (i) synthesis of Cu_2O nanospheres as a sacrificial copper precursor, (ii) solvothermal or hydrothermal conversion to Cu_2MoS_4 nanosheets or nanotube precursors, and (iii) microwave-induced transformation into Cu_2S/MoS_2 epitaxial heterostructures. Each step is described below.

A. Chemicals and materials

Copper(II) chloride ($CuCl_2 \cdot 2H_2O$), polyvinylpyrrolidone (PVP), sodium hydroxide (NaOH), ascorbic acid, sodium molybdate (Na_2MoO_4), thioacetamide (C_2H_5NS), ammonium tetrathiomolybdate ($(NH_4)_2MoS_4$), potassium chloride (KCl), and ethylene glycol ($C_2H_6O_2$) were purchased from Sigma Aldrich. MoS_2 powder (99%, ~325 mesh) was purchased from Alfa Aesar. Microfibrous Al_2O_3 (alumina wool) and quartz tubes were purchased from Thermo Fisher Scientific and AdValue Technology.

B. Synthesis of Cu_2O

The synthesis method for Cu_2O nanospheres was based on previous reports in the literature [39]. Approximately 0.427 g of $CuCl_2 \cdot 2H_2O$ and 8.325 g of PVP (MW = 40 000 g/mol) were dissolved in 250 ml of deionized water. Upon achieving a clear blue solution, approximately 25 ml of 2.0*M* NaOH and 25 ml of 0.6*M* ascorbic acid solutions were added dropwise under constant stirring at room temperature for 2 h. This resulted in the formation of a yellow-orange turbid liquid. The suspension was then centrifuged at 8000 rpm, and the product was washed three times with deionized water and absolute ethanol, followed by drying under vacuum overnight.

C. Synthesis of Cu_2MoS_4 (CMS) nanosheets and nanotube intermediates

Cu_2MoS_4 nanosheets were synthesized through a solvothermal synthesis route. Typically, 20 mg of as-synthesized Cu_2O was dispersed in 20 ml of ethylene glycol. The solution was sonicated for 10 min. 30 mg of sodium molybdate and 60 mg of thioacetamide were added and stirred for 10 min. We then transferred the solution to a 45 ml Teflon-lined autoclave and the mixture was maintained at 200 °C for 24 h. We used $(NH_4)_2MoS_4$ as the precursor for CMS nanotube synthesis. Typically, 45 mg of as-prepared Cu_2O was dispersed in 12 ml of deionized water via sonication for 10 min. Thereafter, 90 mg of $(NH_4)_2MoS_4$ was added to the dispersion, and the mixture was stirred for 30 min. We then transferred the reaction mixture to a 30 ml Teflon-lined autoclave and subjected it to hydrothermal treatment at 120 °C for 4 h. After it was cooled to room temperature, the final products were washed several times with deionized water and ethanol and then dried under vacuum overnight.

D. Cu_2S/MoS_2 heterostructures (nanosheets and nanotubes)

Cu_2S/MoS_2 heterostructures were synthesized via microwave-assisted solid-state heating. Briefly, 0.5 g of as-synthesized CMS nanosheets or nanotubes were weighed and transferred into a round-bottomed quartz tube, which was subsequently packed with alternating layers of Al_2O_3 microfiber and graphite. The prepared tubes were placed in a graphite bath inside an alumina crucible and exposed to microwave irradiation in an instrument equipped with inverter technology (Panasonic, Model NN-SD78LS, 1250 W). The samples were irradiated with microwaves at varying power levels [PWR 1 (<500 °C), PWR 2 (<500 °C), PWR 4 (~500 °C), PWR 6 (~750−800 °C), and PWR 8 (~1000 °C)] for 5 min to facilitate the formation of heterostructures, followed by rapid quenching in water. For conventional high-temperature heating, the as-synthesized Cu_2MoS_4 nanosheets were annealed at different temperatures (300, 400, 500, 600, 800, and 1000 °C)

for 2 h in a tube furnace with a ramp rate of 10 °C/min under a continuous flow of argon gas.

E. Structural and electronic characterization

The crystal structure and phase purity of Cu_2O, CMS, and Cu_2S/MoS_2 heterostructure samples were analyzed via PXRD using a Bruker D8 Advance diffractometer with Cu *K* alpha radiation (1.541 Å). The obtained powder diffraction patterns were compared to patterns in the literature from the Inorganic Crystal Structure Database (ICSD). The morphologies, structures, and bulk composition were observed using an FEI (Hillsboro, OR) Scios 430 nano-SEM scanning electron microscope with an Oxford energy-dispersive x-ray (EDX) detector. Surface composition was investigated using a Kratos Supra Axis x-ray photoelectron spectrometer (Shimadzu corporation) with a monochromatic Al *K* alpha source (1486.6 eV). High-resolution electron microscopy characterization was performed using an FEI Tecnai G2 Twin microscope located at the Shared Materials Instrumentation Facility at Duke University. The microscope was operated at a 200 kV accelerating voltage and was equipped with a GATAN OneView camera. Care was taken to minimize the electron dose to limit beam damage to the samples. Scanning transmission electron microscopy (STEM) characterization was performed using a Thermo Fisher Talos F200X G2 microscope at North Carolina State University. The microscope was operated in STEM mode, with the beam current optimized for collecting energy-dispersive x-ray spectroscopy (EDS) maps. High-angle annular dark field (HAADF) images and EDS maps were collected. Samples were suspended in water and isopropanol via sonication and drop-cast onto Cu and Au carbon-coated TEM grids for HRTEM and STEM imaging, respectively.

F. Electrochemical characterization

All electrochemical testing was conducted in a custom three-electrode H-shaped cell where the working electrode and counter electrode were separated by a Selemion anion exchange membrane. Working electrodes were fabricated using powder-based inks of each catalyst prepared by mixing 5 ml of ethanol, 70 µl of Sustainion ionomer (5 wt % in ethanol), 3 mg of carbon black, and 15 mg of the catalyst powder. Carbon black was used to increase the conductivity, while Sustainion acted as a binder to prevent loss of catalyst from the substrate surface. Inks were sonicated for 45 min, followed by spray depositing 400 µl of ink onto the gas diffusion electrode (Sigracet 36BB). A blank electrode, which was fabricated using ink prepared by mixing 70 µl of Sustainion, 3 mg C black, and 5 ml of ethanol, was used for comparison. Platinum mesh, the Ag/AgCl electrode, and the as-obtained gas diffusion electrode served as counter, reference, and working electrodes, respectively.

All measurements for the hydrogen evolution reaction, to calculate specific capacitance and charge-transfer resistance, were taken in an aqueous Ar-sparged 0.5*M* H_2SO_4 electrolyte. The H_2SO_4 electrolyte was deoxygenated prior to each experiment by purging with Ar for ∼40 min. Linear sweep voltammetry (LSV) experiments were performed at a scan rate of 5 mV/s at room temperature. All electrochemical experiments were performed using a Bio-Logic VSP-300 multichannel potentiostat with potentials converted to the reversible hydrogen electrode (RHE) scale using the following equation:

$$E_{\mathrm{RHE}} = E\ (\mathrm{Ag} - \mathrm{AgCl}) + 0.210 + 0.059 \times \mathrm{pH}.$$

Specific capacitance measurements were made via cyclic voltammetry (CV) in a static solution by sweeping the potential across a non-Faradaic region (∼100 mV potential window centered around the open-circuit potential) at progressively increasing scan rates. A plot of changing current as a function of scan rate yields a linear response, from which per-gram specific capacitance is obtained by dividing the slope by electrode mass loading. Charge-transfer resistance was measured via electrochemical impedance spectroscopy (EIS) at different applied potentials, with a superimposed ac bias oscillating at frequencies ranging from 0.1 to 10 MHz, where impedance data were fitted to a simplified Randles circuit to obtain the charge-transfer resistance values.

The electrolyte used for the electrochemical CO_2 reduction reaction (CO_2RR) was 0.1*M* KOH. The electrolyte was purged with CO_2 for 60 min. The CO_2RR performance was evaluated using the chronoamperometry method at each constant potential. The gaseous and liquid products were quantified by using gas chromatography (GC; equipped with a thermal conductivity detector, TCD) and a Bruker 400 MHz nuclear magnetic resonance (NMR) spectrometer.

III. RESULTS AND DISCUSSION

A. Synthesis and structural characterization

Scheme 1 illustrates a schematic overview of the synthetic route employed to prepare the Cu_2S/MoS_2 nanoheterostructures. This study involves synthesizing Cu_2S/MoS_2 nanoheterostructures via microwave heating of CMS nanosheets and nanotubes previously prepared by solvothermal and hydrothermal methods, respectively. CMS is a bimetallic layered transition-metal sulfide with a band gap of approximately 2.03–2.48 eV [Fig. 1(a)]. It comprises *P* and *I* crystalline phases, corresponding to the $P\bar{4}\bar{2}m$ and $I\bar{4}\bar{2}m$ space groups, respectively [2,40]. These phases are formed through the stacking of van der Waals-interacting single layers of interlinked Cu and Mo atoms, which are tetrahedrally coordinated to bridging sulfur atoms. The atomic arrangement is square planar, with

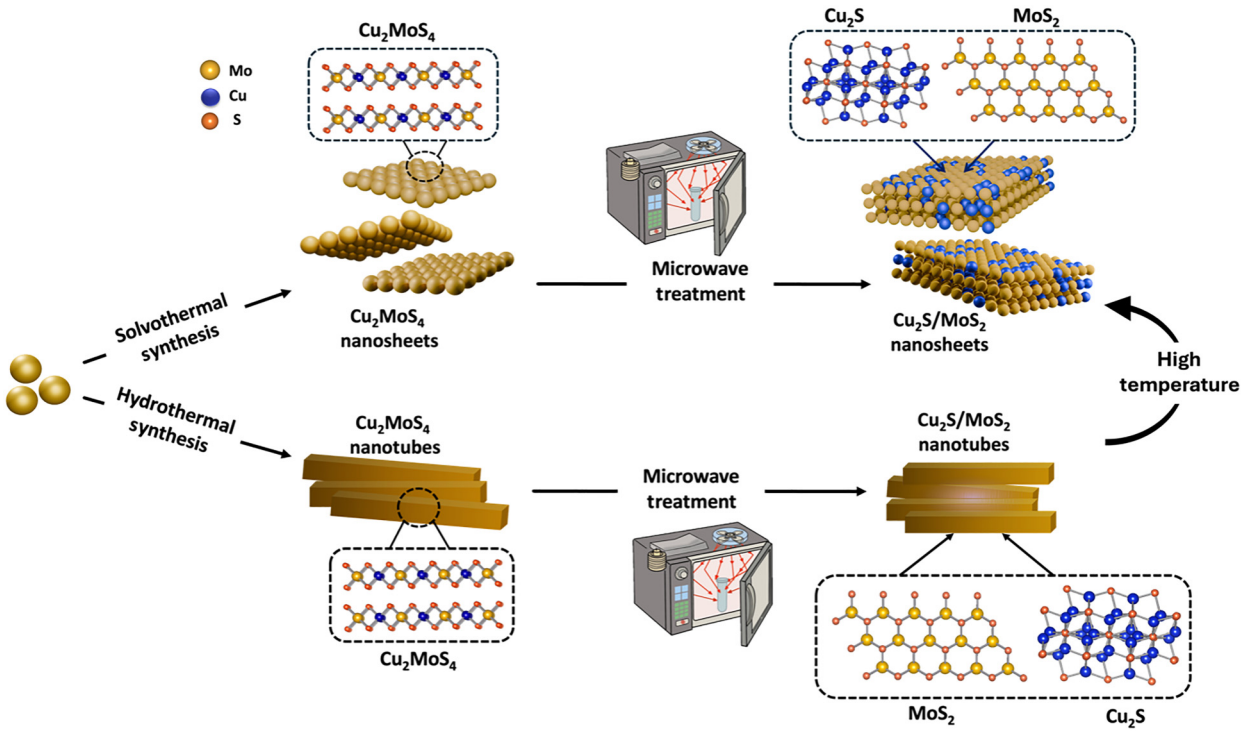

SCHEME 1. Synthetic route for preparing Cu_2S/MoS_2 nanoheterostructures via microwave-assisted transformation of CMS intermediates. CMS nanosheets (nanotubes) are first synthesized via a solvothermal (hydrothermal) route with Cu_2O nanospheres as sacrificial templates, followed by microwave irradiation to induce the formation of Cu_2S/MoS_2 nanosheets and nanotubes.

each sulfur atom coordinating with two copper atoms and one molybdenum atom. The CMS structure is illustrated in Fig. 1(a) [40–43].

First, highly uniform Cu_2O nanospheres [Fig. S1(c) within the Supplemental Material [94]] were employed as a sacrificial template for the synthesis of CMS. Cu_2O nanospheres (Fig. S1 within the Supplemental Material [94]) undergo partial dissolution in ethylene glycol, resulting in the formation of Cu^+ ions. Sodium molybdate dissociates, providing molybdate anions (MoO_4^{2-}). The MoO_4^{2-} anion acts as the Mo precursor and reacts with thioacetamide, which serves as a sulfur source to

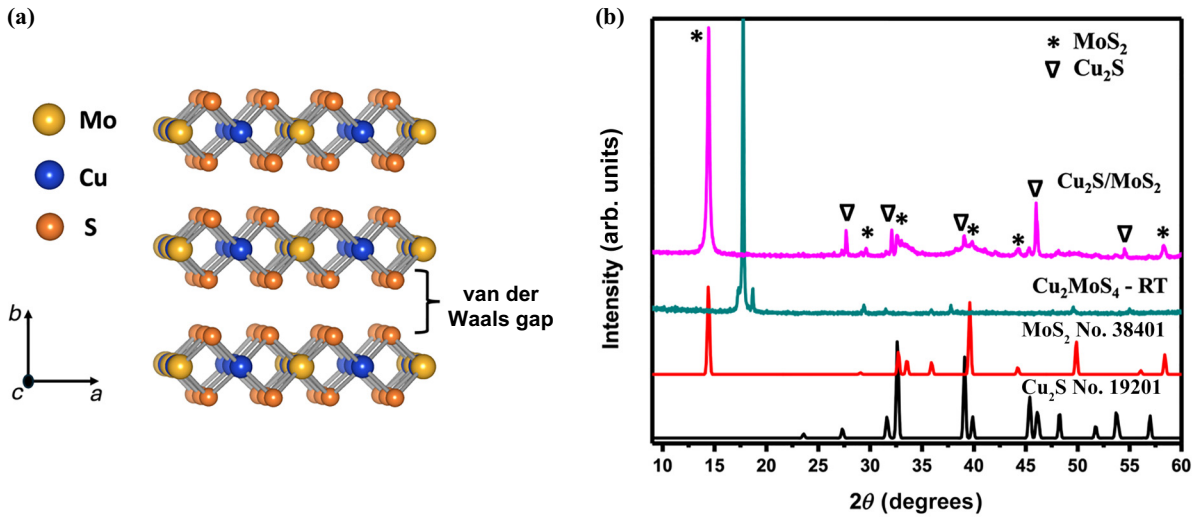

FIG. 1. (a) Crystal structure of *I*-Cu_2MoS_4, (b) experimental diffractogram of the Cu_2S/MoS_2 heterostructure is overlaid with patterns from the ICSD for Cu_2S, MoS_2, and CMS.

form the molybdenum sulfide anion (MoS_4^{2-}). Thioacetamide was used as a sulfur source. When Cu^+ ions react with molybdenum sulfide ions (MoS_4^{2-}), they form CMS sheets via a nucleation and growth process [40,44]. The solvothermal synthesis of CMS nanosheets using ethylene glycol as the solvent, along with the hydrothermal synthesis of nanotubes, exemplifies a solvent-directed approach for controlling morphology. This strategy mainly relies on variations in solvent properties, such as viscosity, dielectric constant, and boiling point [45,46]. The overall reaction can be written as

$$Cu_2O + Na_2MoO_4 + 4C_2H_5NS + H_2O \rightarrow Cu_2MoS_4 + 4CH_3CONH_2 + 2NaOH. \quad (1)$$

Following Cu_2MoS_4 synthesis, the as-obtained nanostructures were then subjected to microwave irradiation, as shown in Scheme 1. These resulted in the formation of Cu_2S/MoS_2 nanoheterostructures, accompanied by the generation of sulfur vapors [47]:

$$Cu_2MoS_4 \rightarrow Cu_2S/MoS_2 + S \uparrow . \quad (2)$$

Figure S1(a) within the Supplemental Material [94] shows the XRD patterns of the as-synthesized Cu_2MoS_4 samples, indicating that the *I*-Cu_2MoS_4 allotrope has been successfully synthesized. SEM analysis confirms a sheetlike morphology with an average edge length of about 1.9 μm, demonstrating high uniformity and no impurities [Fig. S1(b) within the Supplemental Material [94]]. Meanwhile, CMS nanotubes form under hydrothermal conditions when Cu^+ ions from Cu_2O replace NH_4^+ ions in $(NH_4)_2MoS_4$. The different diffusion rates of Cu^+ ions and Mo/S species create vacancies, which drive the Kirkendall effect and ultimately lead to the formation of CMS hollow structures [48].

Powder XRD was utilized to examine the effects of annealing on the as-prepared CMS samples at various microwave power levels (Fig. S2 within the Supplemental Material [94]). As displayed in Fig. 1(b), upon subjecting the CMS nanosheets to microwave treatment, the diffraction peaks can be indexed to the lattice planes of MoS_2 (ICSD No. 38401) and Cu_2S (ICSD No. 19201), confirming the coexistence of both phases. The diffraction peaks observed at room temperature correspond to the *I*-phase Cu_2MoS_4 [Fig. 1(a)].

Similarly, upon microwave irradiation of CMS nanotubes at varying power levels, the resulting PXRD patterns align well with those of MoS_2 and Cu_2S (Fig. S3 within the Supplemental Material [94]).

To further probe the effect of microwave irradiation, the CMS precursor was then subjected to a series of microwave power levels, as shown in Fig. S1 within the Supplemental Material [94]. When the CMS nanosheet

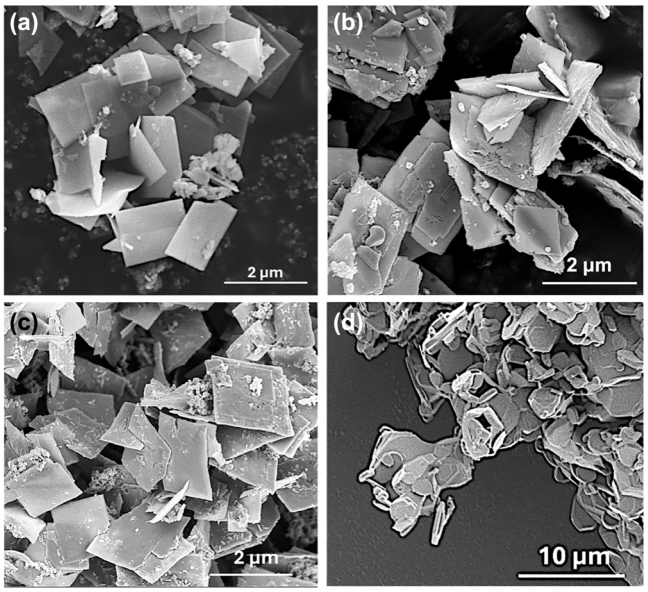

FIG. 2. SEM micrographs of CMS subjected to microwave irradiation at (a) room temperature, (b) power 2, (c) power 4, (d) power 6 for 5 min.

was subjected to microwave irradiation at a power level of 1 (<500 °C), a distinct peak emerged at 14.2°, corresponding to the characteristic peak of the 2*H* phase of MoS_2, while the remaining diffraction peaks remained consistent with the CMS phase. Furthermore, at an annealing power of 2, the formation of MoS_2 and Cu_2S was observed, with these phases remaining dominant as the power increased to the maximum level. Furthermore, the full width at half maximum of the (002) peak of MoS_2 nanosheets exhibited a significant decrease from 0.872 to 0.132 (Fig. S4 within the Supplemental Material [94]) as the annealing power increased from power level 2 to 8, suggesting improved crystallinity and enlarged or agglomerated crystallite domains, as further evidenced in the SEM micrographs [49]. A similar trend was observed when CMS nanotubes were subjected to microwave treatment, exhibiting analogous phase transformations and peak narrowing (Fig. S3 within the Supplemental Material [94]). The PXRD results, therefore, confirm the formation of Cu_2S/MoS_2 nanoheterostructures.

The morphologies and structures of the Cu_2S/MoS_2 heterostructures were examined by FESEM and TEM. As shown in Fig. 2(a), CMS nanosheets synthesized at room temperature display a sheetlike morphology with high uniformity, smooth surfaces, and an average edge length from around 0.8 to 2 μm. Figures 2(b)–2(d) show the FESEM micrographs of the as-prepared Cu_2S/MoS_2 nanoheterostructures obtained after microwave treatment at different power levels (2, 4, and 6). The samples inherit the nanosheetlike morphology and uniformity, but their surfaces become roughened by the formation of

nanowhiskers, resulting in a higher surface roughness than that of the precursor. Such surface texturing is expected to increase the number of exposed active sites [Figs. 2(b) and 2(c)]. At a higher microwave power of level 6, the morphology of the heterostructures evolves into more agglomerated plates [Fig. 2(d)].

A particularly noteworthy morphological evolution was observed when CMS nanotubes were subjected to microwave irradiation. As shown in Fig. S5(a) within the Supplemental Material [94], as-synthesized CMS exhibits well-defined tubular structures at room temperature. Upon microwave treatment at powers 3 and 4 (<500 °C), the nanotubular morphology remained largely intact. However, as microwave irradiation increased to power level 5, a partial transition to sheetlike structures was evident, with residual nanotubes still present. At power level 6 (~750–800 °C), a complete morphological transformation occurred, yielding a uniform sheetlike morphology with an average edge length of approximately 1.8 μm (Fig. S5 within the Supplemental Material [94]). These structural changes are likely driven by the Kirkendall effect, a vacancy-mediated diffusion process that facilitates the nanotube-to-nanosheet transformation under thermal treatment [48]. This process typically occurs through the formation of Kirkendall voids during the reaction of solid nanocrystals, in which the preferential diffusion of atoms or ions from the core material to the reaction interface results in an unbalanced outward material influx. With increasing temperature and annealing time, these voids coalesce near the interface, promoting structural collapse and directional reorganization, minimizing the surface area, and forming a sheetlike structure [40,50,51].

The microstructural characteristics of the Cu_2S/MoS_2 nanoheterostructures were further investigated by FESEM and TEM (Fig. 3). As shown in Fig. 3(a), the SEM image of Cu_2S/MoS_2 prepared at power level 2 reveals a layered structure with a well-defined sheetlike morphology, indicative of MoS_2, interspersed with Cu_2S domains between the layers. The bright-field TEM images [Figs. 3(b) and 3(c)] further reveal the formation of isolated

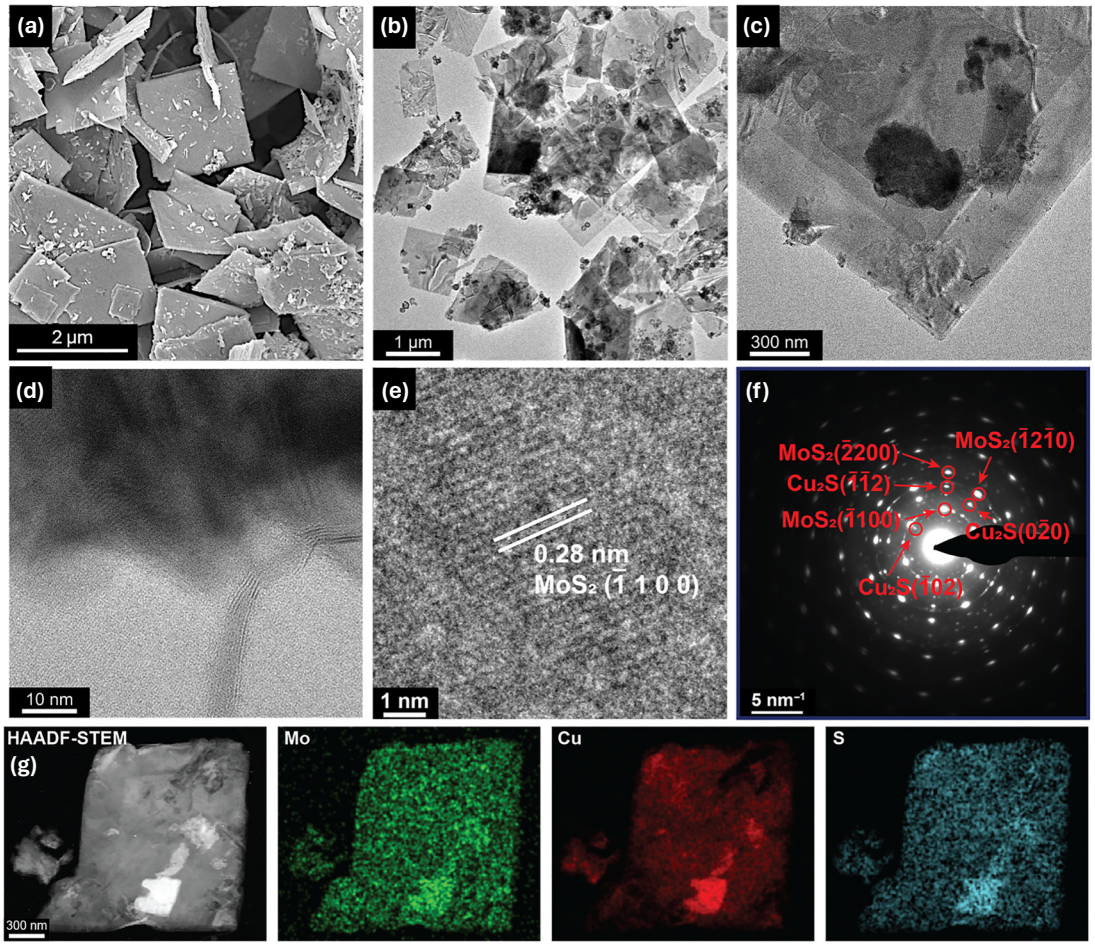

FIG. 3. SEM image of Cu_2S/MoS_2 nanosheets prepared at power level 2 (a); TEM images with scale bars of 1 μm (b) and 300 nm (c), showing the presence of the sheetlike morphology; HRTEM image of Cu_2S/MoS_2 (d),(e); SAED results showing the diffraction spots indicating the presence of Cu_2S and MoS_2 in the nanoheterostructure (f); and STEM-EDS maps for the Cu_2S/MoS_2 nanosheet (g).

sheetlike nanoheterostructures with well-defined lateral dimensions. The observed contrast variations indicate distinct interfacial regions between Cu_2S and MoS_2, where the translucent areas in the TEM images correspond to the exfoliated nature of MoS_2. In contrast, darker domains correspond to Cu_2S, confirming the successful formation of the heterostructure [52]. The lattice-resolved TEM [Fig. 3(d)] image reveals a clear boundary between two distinct crystalline regions, implying the presence of two distinct phases. In the lattice-resolved HRTEM image [Fig. 3(e)], an interplanar spacing of 0.28 nm can be assigned to the $(\bar{1}100)$ crystal plane of MoS_2. The SAED pattern [Fig. 3(f)] shows well-defined diffraction spots corresponding to MoS_2 $(\bar{1}2\bar{1}0)$, $(\bar{2}200)$, and $(\bar{1}100)$ reflections and Cu_2S $(\bar{1}02)$, $(\bar{1}\bar{1}2)$, and $(0\bar{2}0)$ reflections, confirming high crystallinity and phase coexistence. The overlap of diffraction spots with symmetry-related orientations indicates local crystallographic alignment and nanoscale structural coherence at the Cu_2S/MoS_2 interface, consistent with a local epitaxial relationship, where Cu_2S domains nucleate at MoS_2 surfaces with a preferred crystallographic orientation, giving rise to locally coherent heterointerfaces. Structural analysis of both phases via HRTEM is hindered by potential epitaxial growth of Cu_2S on MoS_2, as well as the close similarity in d spacing of crystallographic planes within the two phases. To address this, STEM-EDS mapping was performed [Fig. 3(g)]. The STEM-EDS maps indicate the presence of Mo and Cu throughout the nanosheet structure, with the bright-contrast region in the HAADF image corresponding to Cu-rich domains. Sulfur is uniformly distributed throughout, confirming that the nanoheterostructures are composed homogeneously of Cu, Mo, and S, with the presence of localized copper sulfide crystal domains on the surface. Fast Fourier transform (FFT) analysis reveals a periodic spacing of approximately 3.27 Å, which closely matches the d spacing of the Cu_2S $(\bar{1}02)hkl$ plane, consistent with the zone axis. Additionally, several lattice spacings observed in the HRTEM images range from 2.6 to 2.8 Å, which may correspond to multiple overlapping planes from both Cu_2S and MoS_2. Further characterization of the local epitaxial arrangement of the Cu_2S and MoS_2 domains can be found in Fig. S6 within the Supplemental Material [94]. HRTEM images, SAED patterns, and STEM-EDS maps were collected at the interface between Cu_2S and MoS_2 domains to verify the presence of both phases. Local alignment of the Cu_2S (102) and MoS_2 (1100) lattice fringes was observed, as indicated by HRTEM and FFT band-pass filtered images. The potential crystallographic plane assignments, based on measured d spacings and known structural parameters, can be found in Table S1 within the Supplemental Material [94]. To further elucidate the crystallographic relationship between Cu_2S and MoS_2 in the heterostructure, quantitative texture coefficient (T_{hkl}) analysis was performed on the XRD data using the Harris formula (Table S2 within the Supplemental Material [94]). Both phases exhibit significant and systematic deviation from random powder behavior. MoS_2 shows preferential enhancement of the (101) reflection ($T_{hkl} = 1.744$) with suppression of the (103) reflection ($T_{hkl} = 0.258$), while Cu_2S exhibits strong enhancement of the (201) reflection with corresponding suppression of the (104) reflection. The wide range of T_{hkl} values across reflections in both phases is consistent with a shared crystallographic growth constraint arising from interfacial coupling between two phases (see the Supplemental Material [53,54]).

EDX elemental mapping images of Cu_2S/MoS_2, shown in Fig. S7 within the Supplemental Material [94], indicate that Cu, Mo, and S are uniformly distributed, further supporting the formation of Cu_2S/MoS_2 nanoheterostructures.

To determine the optimal temperature range for Cu_2S/MoS_2 heterostructure formation, temperature-dependent synthesis was performed using a conventional tube furnace. Cu_2MoS_4 precursor samples were annealed at temperatures ranging from 300 to 1000 °C for 2 h under an Ar atmosphere. At 300 °C, the diffraction peaks correspond to the Cu_2MoS_4 phase, indicating no decomposition occurs at this temperature (Fig. S8 within the Supplemental Material [94]). Upon increasing the temperature to 400 °C, characteristic peaks of both Cu_2S and MoS_2 begin to emerge, while Cu_2MoS_4 peaks diminish in intensity, suggesting the onset of phase transformation.

To assess the versatility of our microwave-assisted strategy beyond Cu-based systems, we applied the same synthetic framework to construct ZnS/MoS_2 heterostructures. This effort serves to demonstrate that interfacial engineering via rapid microwave transformation can be extended to other transition-metal sulfides, further validating the generalizability of the method. ZnS/MoS_2 heterostructures were synthesized using a comparable reaction methodology, by exposing $ZnMoS_4$ to microwave irradiation at power level 5 (625 W, ∼600–700 °C) for a duration of 5 min. The crystal structure of the as-synthesized samples was analyzed using PXRD. The diffraction peaks in ZnS/MoS_2 at 26.9°, 28.5°, 30.5°, 47.4°, 51.6°, and 56.2° are indexed to the (100), (002), (101), (110), (103), and (112) crystal planes of ZnS (ICSD No. 67453), while reflections at 14.4°, 28.5°, 32.83°, and 58.34° are indexed to the (002), (004), (100), and (110) planes of MoS_2 (ICSD No. 38 401) [Fig. 4(a)]. These results confirm the coexistence of both ZnS and MoS_2 phases, demonstrating the successful formation of the ZnS/MoS_2 heterostructure. SEM analysis further reveals that the ZnS/MoS_2 heterostructure exhibits a microrodlike morphology with lengths ranging from 5 to 10 μm [Fig. 4(b)]. Further SEM-EDS mapping reveals the homogeneous spatial distribution of Zn, Mo, and S throughout the sample [Fig. 4(c)]. This approach thus establishes a facile and generalizable microwave-assisted strategy for the rapid

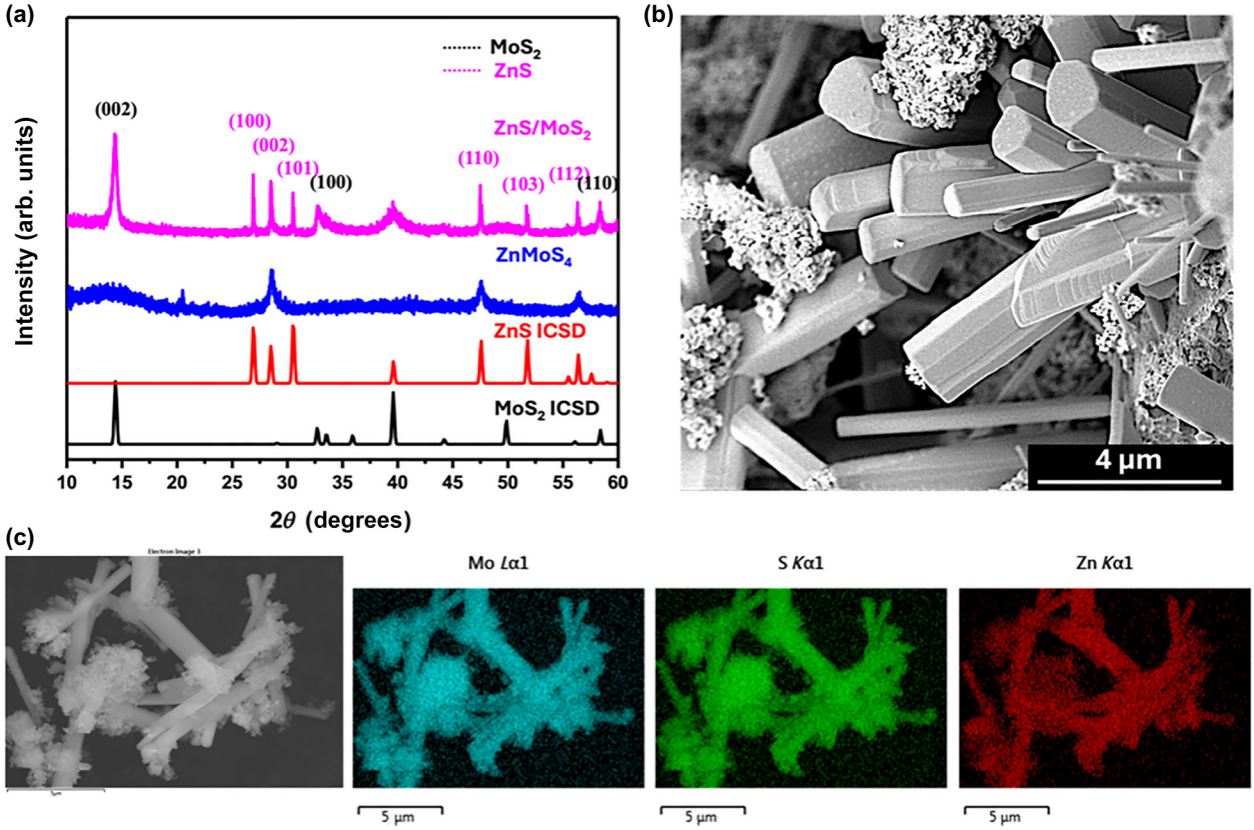

FIG. 4. Experimental diffractograms are overlaid with patterns from the ICSD for MoS_2, ZnS, $ZnMoS_4$, and ZnS/MoS_2. (b) SEM micrograph of the as-synthesized ZnS/MoS_2 heterostructure, (c) SEM-EDS mapping of the ZnS/MoS_2 heterostructure.

synthesis of metal sulfide-MoS_2 heterostructures. These results demonstrate that the synthetic principles established for Cu_2S/MoS_2, particularly morphology control via microwave power modulation and local epitaxial interfacial development, are applicable to other metal sulfide systems, supporting the broader potential of this approach for heterostructure design.

The chemical composition of Cu_2S/MoS_2 was further analyzed and compared with those of CMS and MoS_2 using XPS, as shown in Fig. 5. The as-prepared CMS sample at room temperature shows the Mo $3d_{3/2}$ and Mo $3d_{5/2}$ peaks at 234.34 and 232.48 eV, respectively, whereas the S $2p_{1/2}$ and S $2p_{3/2}$ peaks are found at 163.04 and 161.05 eV, respectively, and those of Cu $2p_{1/2}$ and Cu $2p_{3/2}$ are at 951.75 and 931.86 eV, respectively. These binding energies are consistent with Mo^{6+}, S^{2-}, and Cu^{+}, respectively (Fig. 5). Upon microwave treatment, all samples exhibited a slight increase in binding energies, indicating the formation of new phases and possible changes in the electronic environment of the constituent elements [47].

The low oxygen concentration detected in the survey spectra of all the samples likely results from surface oxidation due to exposure to air [55]. As shown in Fig. 5(a), the Mo $3d$ spectra of Cu_2MoS_4 (i), Cu_2S/MoS_2 (ii), and MoS_2 sheets (iii) reveal clear distinctions. For Cu_2S/MoS_2 (ii), the peaks at 229.8 and 232.6 eV correspond to the Mo^{4+} $3d_{5/2}$ and Mo^{4+} $3d_{3/2}$ states, respectively, which are characteristic of MoS_2. Additional peaks at higher energies of 233.6 and 235.2 eV are attributed to Mo^{6+}, likely arising from partial surface oxidation upon exposure to air [37]. The high-resolution Mo $3d$ spectrum also exhibits a peak at 225.3 eV, associated with the S $2s$ orbital. Figure 5(b) shows the S $2p$ profiles of Cu_2MoS_4 (i), Cu_2S/MoS_2 (ii), and MoS_2 sheets (iii), where the S $2p$ spectrum of Cu_2S/MoS_2 (ii) can be deconvoluted into two peaks of $2p_{1/2}$ and $2p_{3/2}$ at 163.8 and 162.7 eV, which correspond to the S^{2-} anion, which is closely matched to MoS_2 [37,56]. The deconvoluted Cu $2p$ XPS spectrum of Cu_2S/MoS_2 [Fig. 5(c)] shows distinct peaks at 952.69 and 932.94 eV, assigned to Cu^{+} $2p_{1/2}$ and Cu^{+} $2p_{3/2}$, respectively, along with additional peaks at 954.52 and 935.22 eV, which are assigned to Cu^{2+} $2p_{1/2}$ and Cu^{2+} $2p_{3/2}$, respectively, of Cu_2S/MoS_2 (ii). The Mo $3d$ peaks in the Cu_2S/MoS_2 heterojunction exhibit a slight shift to a higher binding energy than that of MoS_2, indicative of electron migration from MoS_2 to Cu_2S. Meanwhile, the S $2p_{3/2}$ peak of Cu_2S/MoS_2, with a binding energy of 163.86 eV, demonstrates a negative shift of 0.3 eV compared to pristine MoS_2 sheets. These observations provide evidence of clear electronic interactions between

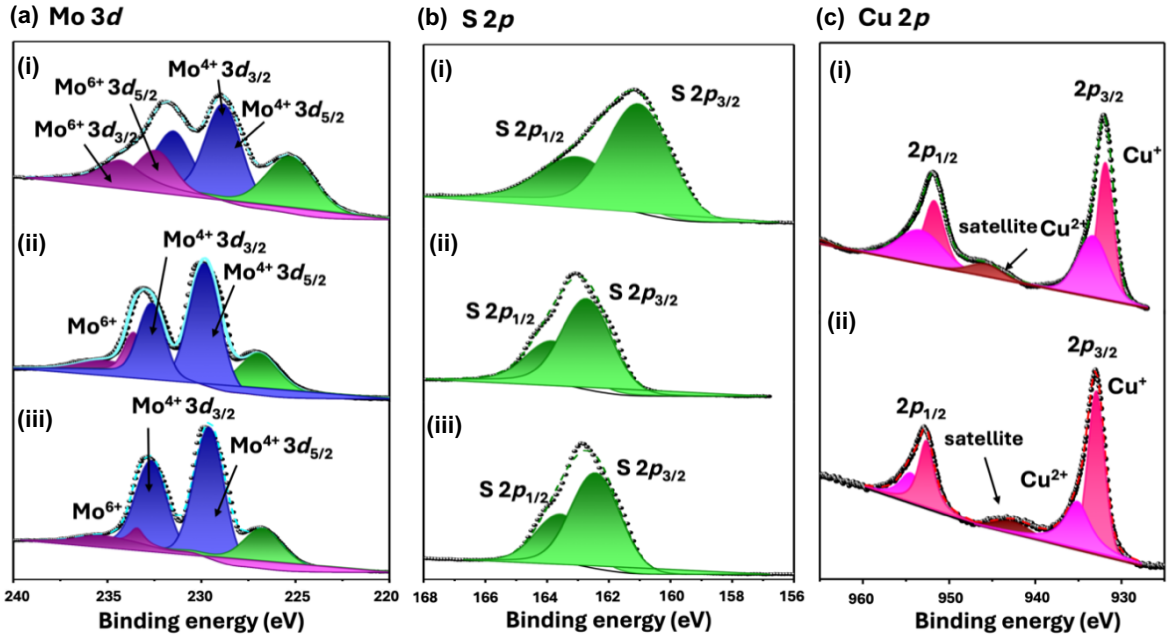

FIG. 5. High-resolution XPS spectra of Mo 3*d* (a), S 2*p* (b), and Cu 2*p* (c) of CMS nanosheets (i), Cu_2S/MoS_2 nanosheets (ii), and MoS_2 (iii).

Cu_2S and MoS_2 lattices, indicating the successful formation of a Cu_2S/MoS_2 heterojunction with substantial interfacial charge redistribution and well-defined coupling interfaces [55,57]. This could enhance interfacial electric fields that promote efficient charge separation during catalytic processes. Furthermore, the coexistence of Cu^+/Cu^{2+} and Mo^{4+}/Mo^{6+} species also shows a dynamic redox environment, potentially contributing to improved electrocatalytic activity through electron-transfer pathways at the Cu-Mo-S interfaces.

To further examine the electronic structure of the heterostructure, the projected density of states (PDOS) were calculated (see Note 2 within the Supplemental Material [94] for details [58–63]) and are plotted in Fig. 6(a). In pristine MoS_2, the PDOS exhibit semiconducting behavior with a pronounced gap in the density of states at the Fermi level. The PDOS of the Cu_2S/MoS_2 nanoheterostructure show Cu (purple) states increasing the density of states near the valence band, indicating that the Cu_2S layer introduces electronic density near the Fermi level of the

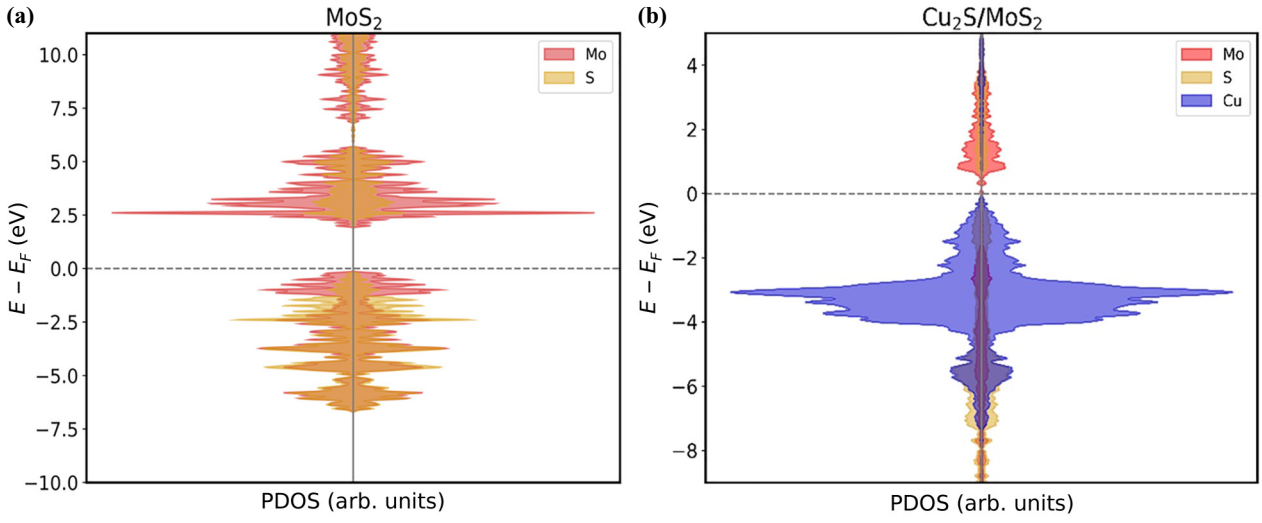

FIG. 6. Calculated PDOS for MoS_2 (a) and the Cu_2S/MoS_2 heterostructure (b). PDOS includes only the metal *d* states and sulfur *p* states. Dashed gray line marks the Fermi energy level (E_F).

heterostructure, leading to narrowing of the band gap from 2.2098 eV in MoS_2 to 0.0427 eV in the Cu_2S/MoS_2 heterostructure. It shows overlapping distributions of Cu and Mo states just below the Fermi level, demonstrating hybridization between the Cu 3*d* and Mo 4*d*/S 2*p* orbitals at the interface. This hybridization facilitates efficient charge transfer across the interface. The catalytic activity of the nanoheterostructures is attributed to strong interfacial electronic coupling, which induces a pronounced *d*-*d* orbital interaction between the Cu 3*d* and Mo 4*d* states, thereby enhancing the overall activity [64]. Such interfacial coupling has been demonstrated to modulate the electronic structure by creating active interfacial sites, increasing the charge-carrier density, and resulting in a metallic character [65].

B. Electrochemical analysis

1. Hydrogen evolution reaction (HER)

The electrochemical HER activity of the Cu_2S/MoS_2 nanoheterostructures was evaluated in Ar-saturated 0.5*M* H_2SO_4 solution using a standard three-electrode setup (Fig. S9 within the Supplemental Material [94]). For comparison, the HER activities of CMS nanosheets, CMS nanotubes, and blank electrodes were also measured under identical conditions. Figure 7(a) shows the polarization curves of the as-prepared samples at a scan rate of 5 mV/s. CMS nanosheets and nanotubes exhibited relatively poor HER performance with overpotentials of 370 and 310 mV, respectively, at a current density of 10 mA cm^{-2}. Interestingly, the Cu_2S/MoS_2 nanoheterostructures exhibit a distinct electrochemical response, likely due to interfacial modification of the electronic structure. Cu_2S/MoS_2 nanotubes had a lower overpotential of 252 mV, while Cu_2S/MoS_2 nanosheets had an overpotential of 295 mV at η_{10} [Fig. 7(a)]. This result underscores the significance of interfacial coupling in promoting synergistic effects between Cu_2S and MoS_2 [48,66]. The enhanced activity of nanotubular heterostructures with well-defined inner cavities underscores the significance of morphology. Hollow architectures could provide higher surface areas, enhanced exposure of accessible active sites, and shorter charge-transport pathways, collectively improving the HER kinetics and electrocatalytic activity [67,68].

To evaluate the electrochemical surface area (ECSA), the double-layer capacitance (C_{DL}) is determined by conducting multiple CV measurements in the non-Faradaic region as a function of scan rate, since the ECSA scales linearly with C_{DL}. Based on the fitting results between the density difference (Δj) and scan rate in the CV curves, shown in Fig. 7(b), the C_{DL} values are calculated to be 3.24, 2.91, 2.48, and 1.31 mF cm^{-2} for Cu_2S/MoS_2

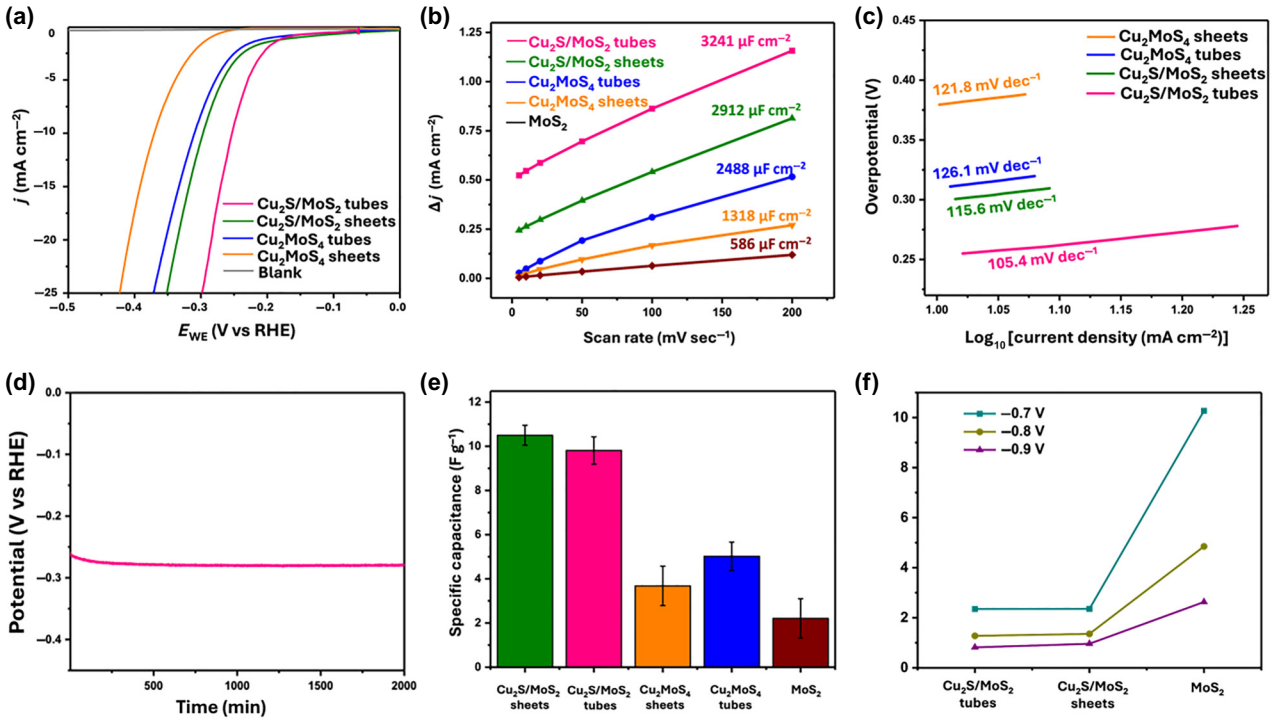

FIG. 7. HER characterization. (a) Polarization curves for Cu_2S/MoS_2 nanotubes (PWR 4), Cu_2S/MoS_2 nanosheets (PWR 2), CMS nanotubes, CMS nanosheets, and blank in 0.5*M* H_2SO_4; (b) ECSA calculation using C_{DL} for the samples studied; (c) Tafel plots of polarization curves of all samples studied; (d) stability test; (e) specific capacitance per gram; and (f) charge-transfer resistance for proton reduction of Cu_2S/MoS_2 nanotubes, Cu_2S/MoS_2 nanotubes, CMS nanosheets, CMS nanosheets, and MoS_2.

nanotubes, Cu_2S/MoS_2 nanosheets, CMS nanotubes, and CMS nanosheets, respectively. These values closely relate to the HER activities.

The Tafel slopes derived from LSV plots further provide insights into the reaction mechanism and rate-determining step of the HER. In acidic media, the HER proceeds via two possible mechanisms. The Volmer-Heyrovsky pathway involves proton adsorption, followed by reduction to form H^+, which then reacts with an electron and a second proton to form H_2. Alternatively, the Volmer-Tafel route involves proton adsorption followed by reduction and then recombination with a neighboring H^* to form H_2 [69,70]. The measured Tafel slopes are 105.4, 115.6, 121.8, and 126.1 mV dec^{-1} for Cu_2S/MoS_2 nanotubes, Cu_2S/MoS_2 nanosheets, CMS nanosheets, and CMS nanotubes, respectively [Fig. 7(c)]. The Tafel slope indicates that Cu_2S/MoS_2 nanotubes and nanosheets follow a Volmer-Heyrovsky mechanism, where electrochemical desorption via proton-coupled electron transfer governs H_2 evolution [71]. The Tafel slope of over 120 mV dec^{-1} for CMS nanotubes and nanosheets suggests the Volmer step as the rate-determining step under acidic conditions.

The specific capacitance of all the samples was determined via cyclic voltammetry by sweeping the potential within the non-Faradaic region. A linear plot of current density versus scan rate was used to determine the double-layer capacitance (C_{DL}), from which the gravimetric specific capacitance was calculated by normalizing the slope with respect to the electrode mass loading (Figs. S10 and S11 within the Supplemental Material [94]). Cu_2S/MoS_2 nanosheets synthesized at power level 2 (<500 °C) exhibited the highest gravimetric specific capacitance of 10.50 ± 0.45 F g^{-1}, demonstrating the highest specific capacitance compared to Cu_2S/MoS_2 nanotubes, CMS nanosheets, CMS nanotubes, and MoS_2 at 9.81 ± 0.62, 3.68 ± 0.89, 5.02 ± 0.64, and 2.21 ± 0.26 F g^{-1}, respectively [Fig. 7(e)]. MoS_2 nanosheets possess a high specific surface area and intrinsically fast ionic conductivity; however, they suffer from easy stacking and aggregation, which weakens the material's inherent advantages. The integration of Cu_2S not only mitigates MoS_2 restacking but also induces sulfur vacancies, thereby exposing more electroactive edge sites and enhancing the specific capacitance [72,73].

EIS measurements were conducted to further probe the charge-transfer kinetics. Figures S12(a)–S12(c) within the Supplemental Material [94] show individual Nyquist plots of the as-prepared Cu_2S/MoS_2 nanotubes, Cu_2S/MoS_2 nanosheets, and MoS_2, which were examined at open-circuit voltage. These semicircular Nyquist plots suggested that the interfacial electron-transfer processes could be effectively described by a simplified Randles equivalent circuit comprising a solution resistance (R_s), a charge-transfer resistance (R_{CT}), and a double-layer capacitance (C_{DL}) (Fig. S13 within the Supplemental Material [94]). The Nyquist plots shown in Fig. S12 within the Supplemental Material [94] display a small potential-independent semicircle at high frequencies and a larger potential-dependent semicircle at lower frequencies [74,75]. The potential-independent semicircle corresponds to contact between the gas diffusion electrode and the catalyst, while the potential-dependent larger semicircle reflects the charge-transfer resistance [75,76]. As shown in Fig. 7(f), the charge-transfer resistance (R_{CT}) values for all samples decreased from 2.35 to 0.95 Ω with increasing reductive potential from −0.7 to −0.9 V, for Cu_2S/MoS_2 nanotubes. Similarly, for Cu_2S/MoS_2 nanosheets, the R_{CT} values dropped from 2.35 to 0.95 Ω, and for MoS_2, they decreased from 10.27 to 2.63 Ω. The smaller R_{CT} value for Cu_2S/MoS_2 nanotubes correlates well with their lower overpotential, reflecting an enhanced propensity for proton reduction and indicating a faster Faradaic process in terms of HER kinetics.

Electrochemical stability was assessed through chronopotentiometry at a constant current density of 10 mA cm^{-2} for 2000 min to observe the overpotential as a function of electrolysis time. Figure 7(d) shows that Cu_2S/MoS_2 nanotubes demonstrated stability in acidic media, maintaining a negligible potential deviation during the operation test.

2. Electrochemical CO_2 reduction (CO_2RR)

The electrochemical CO_2RR of Cu_2S/MoS_2 nanoheterostructures was evaluated in a sealed electrochemical H-cell containing 0.1*M* KOH electrolyte (Fig. S9 within the Supplemental Material [94]). The liquid and gaseous products were analyzed via ^1H NMR and GC-TCD, respectively. As shown in Fig. 8(a), the LSV curves of Cu_2S/MoS_2 show an increased current density under CO_2 saturation compared to Ar, indicating activity towards the CO_2RR. Chronoamperometry experiments were subsequently performed on Cu_2S/MoS_2 nanosheets and nanotubes at −0.34 and −0.44 V versus RHE, respectively, to evaluate their product distribution. Figures 8(b) and 8(c) illustrate the product selectivity of Cu_2S/MoS_2 nanosheets, demonstrating Faradaic efficiencies (FEs) of approximately 3% and 2.5% towards formate production at applied potentials of −0.44 and −0.34 V versus RHE, respectively, while Cu_2S/MoS_2 nanotubes exhibited FEs of 3.5% and 0.8% under similar conditions, at applied potentials of −0.44 and −0.34 V versus RHE, respectively. In all cases, hydrogen evolution dominated the reaction, accounting for >90% of the total FE, reflecting the kinetic favorability of hydrogen evolution in aqueous media and acting as a competing reaction, thereby reducing the overall efficiency. Additionally, significant mass transport limitations in aqueous static cells arise from the sluggish diffusion rate of CO_2 in aqueous electrolyte [77–79]. The Faradaic efficiencies of the detected

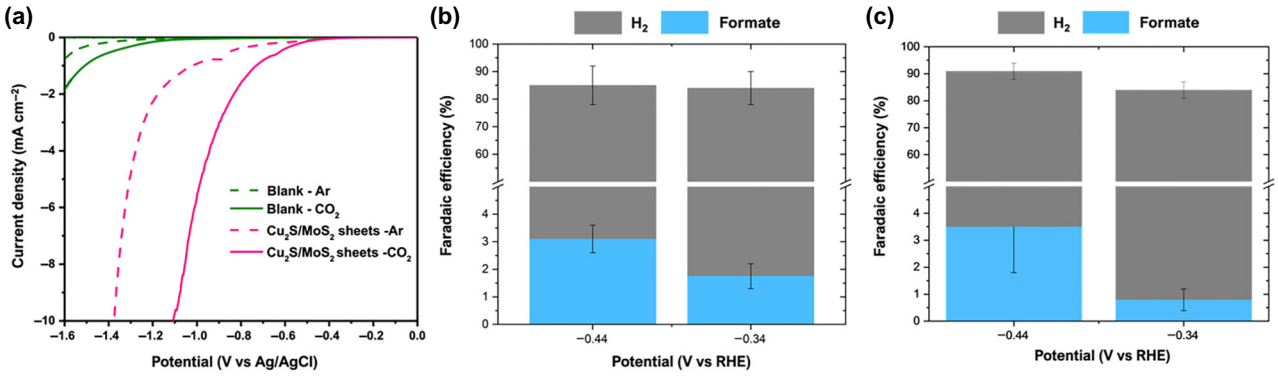

FIG. 8. (a) Linear sweep voltammograms in Ar- and CO_2-enriched atmospheres, (b) Faradaic efficiencies for CO_2 reduction on Cu_2S/MoS_2 nanosheets, and (c) Cu_2S/MoS_2 nanotubes in 0.1*M* KOH electrolyte.

products were generally close to 100%, with minor discrepancies likely attributed to electrode surface oxidation or partial corrosion during electrolysis [31,80,81]. Electrochemical CO_2 reduction served as a sensitive probe to detect changes in interfacial charge redistribution, suggesting that the modest formate yield reflected altered intermediate stabilization rather than optimized catalytic selectivity. Formate selectivity remains modest (∼3−4%). However, optimization of the catalyst loading, electrolyte composition, and electrode architecture may improve the CO_2 reduction performance in future studies.

Although pristine MoS_2 exhibits limited intrinsic activity for formate generation, we believe the synergistic interaction between MoS_2 and Cu_2S, which induces interfacial electronic coupling, could enhance its activity and stability for formate production during the CO_2RR. The selectivity towards formate production arises from the relative energetics of the two-electron reduction CO_2RR pathways, forming either $CO + H_2$ or formate. CO production is believed to follow a carbophilic pathway via carboxyl ($COOH^*$) intermediates, while formate production is expected to proceed via an oxophilic pathway involving formyloxyl ($OCHO^*$) intermediates [82,83]. The first step of the CO_2RR for formate production is CO_2 hydrogenation via a proton-electron pair ($H^+ + e^-$) transfer to form the *OCHO intermediate:

$$H^+ \text{ attacks the C atom} : {}^* + CO + H^+ + e^- \rightarrow {}^*OCHO.$$

The subsequent hydrogenation step leads to the formation of HCOOH. On the Cu_2S/MoS_2 interface, $^*CO_2$ preferentially hydrogenates to *OCHO on the Cu_2S/MoS_2 interface due to the formation of a Cu–O bond, whereas in the case of pristine MoS_2, this step is not favorable due to the high Gibbs free energy barrier. The electronegativity difference between Cu and Mo drives the electron transfer from Cu_2S to MoS_2, modulating the *d*-band center and potentially lowering the energy barrier for CO_2 adsorption and activation [84].

Density functional theory (DFT) calculations were used to evaluate the favorability of *OCHO formation on Cu_2S/MoS_2 surface sites (see Note 1 within the Supplemental Material [94] for details [58–60,85–93]). On the Cu_2S surface, the formate (*OCHO) intermediate binds strongly (computed binding energy ≈ –0.77 eV), while the carboxyl (*COOH) intermediate is moderately stabilized (≈ –0.58 eV). In contrast, the adsorption of CO and CO_2 on Cu_2S is weak, with binding energies of only –0.31 and –0.23 eV, respectively. In contrast, MoS_2 displays a negligible interaction with the intermediates; even the CO_2 species is only very weakly adsorbed (≈–0.12 eV; Fig. 9). These results indicate that the Cu_2S surface provides strong stabilization for key CO_2 reduction intermediates (especially *OCHO and *COOH), whereas the MoS_2 surface is largely inert towards binding these molecules (Figs. S14 and S15 within the Supplemental

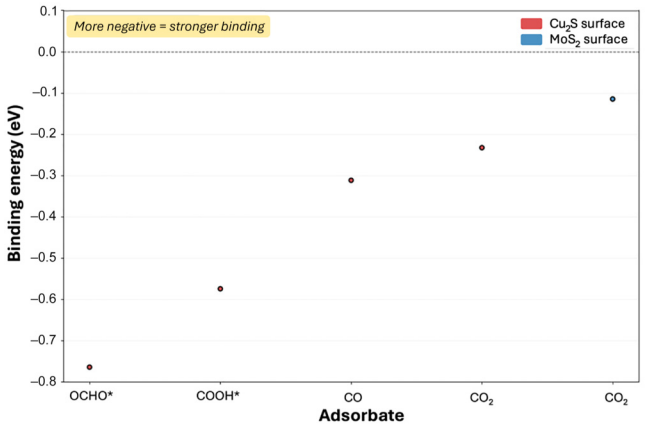

FIG. 9. Binding energies of CO_2 reduction intermediates on Cu_2S and MoS_2 surfaces (the binding energies shown represent the lowest binding energy for each intermediate across several possible sites).

Material [94]). These results underscore Cu_2S as the probable active phase responsible for intermediate stabilization and integration with MoS_2 offers potential future avenues to stabilize the key intermediate, ultimately enhancing both electron transfer and catalytic efficiency.

The structural and compositional stability of the catalyst after electrolysis was assessed by pre- and postanalysis. The PXRD pattern for the Cu_2S/MoS_2 electrode shows no discernible shifts in peak positions or intensity, confirming the structural robustness of the nanoheterostructure before and after electrolysis, as shown in Fig. S16 within the Supplemental Material [94]. Similarly, SEM images indicate no significant changes to the morphology or distribution of the catalyst on the surface over the course of electrolysis, whereas postelectrolysis XPS spectra reveal a consistent composition of the catalyst, as shown in Figs. S17 and S18 within the Supplemental Material [94].

IV. CONCLUSIONS

This study establishes that Cu_2S/MoS_2 heterostructures exhibit local structural coherence at nanoscale interfaces, as evidenced by HRTEM and SAED. The use of rapid microwave synthesis provides a durable and scalable approach for producing morphology-controlled Cu_2S/MoS_2 nanoheterostructures, offering a versatile protocol applicable to other metal sulfide-MoS_2 systems. SAED and HRTEM analyses suggest local coherent alignment between Cu_2S and MoS_2, indicating the formation of a local coherent interface. XPS analysis shows that the heterogeneous interfaces of Cu_2S/MoS_2 encourage efficient charge transfer between the components and boost electronic conductivity through built-in interfacial electric fields. Electrochemical reactions were employed as diagnostic probes to interrogate interfacial charge redistribution, arising from synergistic interactions within Cu_2S/MoS_2, rather than as benchmarks of catalytic performances. The observed shifts in electrochemical response and reaction intermediates reflect how the local interfacial registry modulates the electronic structure and charge transfer, providing insights into structure-function relationships in coupled sulfide heterostructures. Furthermore, experimental results and DFT calculations indicate a measurable shift in CO_2 reduction selectivity toward formate at a lower overpotential of -0.34 V versus RHE, underscoring the potential of heterointerface engineering to advance next-generation electrocatalysts. DFT calculations reveal that interfacial coupling in the Cu_2S/MoS_2 nanoheterostructure leads to a redistribution of electronic states near the Fermi level, in agreement with the observed charge transfer. The successful extension of this synthetic strategy to ZnS/MoS_2 further highlights the generalizability of microwave-assisted interfacial engineering for diverse transition-metal sulfide systems.

ACKNOWLEDGMENTS

We thank the National Science Foundation for support through the Faculty Early Career Development Program (DMR2044403) and the Center for Closing the Carbon Cycle, an Energy Frontier Research Center funded by the U.S. Department of Energy, Office of Science, Basic Energy Sciences, under Award No. DE-SC0023427. Additionally, we also acknowledge funding support from the Camille Dreyfus Teacher-Scholar Awards Program (TC-22-096) and the Alfred P. Sloan Foundation Award (FG-2023-203903). S.A.V. acknowledges support from a National Science Foundation graduate research fellowship under Grant No. DGE-2139754. This work was performed in part at the Duke University Shared Materials Instrumentation Facility (SMIF), a member of the North Carolina Research Triangle Nanotechnology Network, which is supported by the National Science Foundation (Award No. ECCS-2025064) as part of the National Nanotechnology Coordinated Infrastructure (NNCI). This work was performed in part at the Analytical Instrumentation Facility (AIF) at North Carolina State University, which is supported by the State of North Carolina and the National Science Foundation (Award No. ECCS-2025064). The AIF is a member of the North Carolina Research Triangle Nanotechnology Network, a site in the National Nanotechnology Coordinated Infrastructure (NNCI).

DATA AVAILABILITY

The data that support the findings of this article are openly available.

[1] E. Pomerantseva and Y. Gogotsi, Two-dimensional heterostructures for energy storage, Nat. Energy **2**, 17089 (2017).

[2] X. Ouyang, B. Huo, S. Peng, M. Xu, D. Deng, Y. Li, and L. Luo, Heterojunction $CuS@Cu_2MoS_4$ nanocubes for nonenzymatic electrochemical glucose sensing, ACS Appl. Nano Mater. **8**, 7132 (2025).

[3] A. Li, X. Chang, Z. Huang, C. Li, Y. Wei, L. Zhang, T. Wang, and J. Gong, Thin heterojunctions and spatially separated cocatalysts to simultaneously reduce bulk and surface recombination in photocatalysts, Angew. Chem., Int. Ed. Engl. **55**, 13734 (2016).

[4] K. Chen, X. Wan, J. Wen, W. Xie, Z. Kang, X. Zeng, H. Chen, and J.-B. Xu, Electronic properties of MoS_2–WS_2 heterostructures synthesized with two-step lateral epitaxial strategy, ACS Nano **9**, 9868 (2015).

[5] J. W. Fu, J. G. Yu, C. J. Jiang, and B. Cheng, *g*-C3N4-based heterostructured photocatalysts, Adv. Energy Mater. **8**, 1701503 (2018).

[6] S. Gbadamasi, M. Mohiuddin, V. Krishnamurthi, R. Verma, M. W. Khan, S. Pathak, K. Kalantar-Zadeh, and N. Mahmood, Interface chemistry of two-dimensional heterostructures – fundamentals to applications, Chem. Soc. Rev. **50**, 4684 (2021).

[7] P. Aggarwal, D. Sarkar, P. K. Dwivedi, P. W. Menezes, and K. Awasthi, Deciphering the influence of morphology and crystal structure on alkaline hydrogen evolution activity in polymorphic cobalt diselenide, ACS Appl., Energy Mater. **7**, 1550 (2024).

[8] J. Linnemann, K. Kanokkanchana, and K. Tschulik, Design strategies for electrocatalysts from an electrochemist's perspective, ACS Catal. **11**, 5318 (2021).

[9] X. Peng, Y. Yan, X. Jin, C. Huang, W. Jin, B. Gao, and P. K. Chu, Recent advance and prospectives of electrocatalysts based on transition metal selenides for efficient water splitting, Nano Energy **78**, 105234 (2020).

[10] J. Zhang, S. Xia, Y. Wang, J. Wu, and Y. Wu, Recent advances in dynamic reconstruction of electrocatalysts for carbon dioxide reduction, iScience **27**, 110005 (2024).

[11] Z. Zhang, P. Chen, X. Duan, K. Zang, J. Luo, and X. Duan, Robust epitaxial growth of two-dimensional heterostructures, multiheterostructures, and superlattices, Science **357**, 788 (2017).

[12] Weiqing Zhang and Xianmao Lu, Morphology control of bimetallic nanostructures for electrochemical catalysts, Nanotechnol. Rev. **2**, 1 (2013).

[13] Q. Li, G. Fang, Z. Wu, J. Guo, Y. You, H. Jin, and J. Wan, Advanced microwave strategies facilitate structural engineering for efficient electrocatalysis, ChemSusChem **17** , e202301874 (2024).

[14] Y. You, G. Fang, M. Fan, J. Guo, Q. Li, and J. Wan, Leveraging novel microwave techniques for tailoring the microstructure of energy storage materials, Microstructures **4**, 2024035 (2024).

[15] J. C. Ortiz-Rodríguez and J. M. Velázquez, Structure–reactivity relationships in Chevrel phase electrocatalysts for small-molecule reduction reactions, Curr. Opin. Electrochem. **34**, 101002 (2022).

[16] Z. Chen, X. Wang, J. P. Mills, C. Du, J. Kim, J. Wen, and Y. A. Wu, Two-dimensional materials for electrochemical CO_2 reduction: Materials, *in situ*/*operando* characterizations, and perspective, Nanoscale **13**, 19712 (2021).

[17] N. Hussain, M. A. Abdelkareem, H. Alawadhi, K. Elsaid, and A. Olabi, Synthesis of Cu-*g*-C_3N_4/MoS_2 composite as a catalyst for electrochemical CO_2 reduction to alcohols, Chem. Eng. Sci. **258**, 117757 (2022).

[18] Q. Yun, L. Li, Z. Hu, Q. Lu, B. Chen, and H. Zhang, Layered transition metal dichalcogenide-based nanomaterials for electrochemical energy storage, Adv. Mater. **32**, 1903826 (2020).

[19] P. Kour, Deeksha, S. Kour, A. L. Sharma, and K. Yadav, MoS_2-based core-shell nanostructures: Highly efficient materials for energy storage and conversion applications, J. Energy Storage **66**, 107393 (2023).

[20] D. Lal, T. Konnur, A. M. Verma, M. Shaneeth, and A. Govind Rajan, Unraveling low overpotential pathways for electrochemical CO_2 reduction to CH_4 on pure and doped MoS_2 edges, Ind. Eng. Chem. Res. **62**, 21191 (2023).

[21] R. Ganatra and Q. Zhang, Few-layer MoS_2: A promising layered semiconductor, ACS Nano **8**, 4074 (2014).

[22] P. Fu, Y. Xu, P. Ge, X. Li, J. Yang, G. Ge, and X. Yang, Highly efficient MoS_2/WS_2 heterojunctions for the CO_2 reduction reaction: Strong electronic transmission, Phys. Chem. Chem. Phys. **25**, 32093 (2023).

[23] Z. He and W. Que, Molybdenum disulfide nanomaterials: Structures, properties, synthesis and recent progress on hydrogen evolution reaction, Appl. Mater. Today **3**, 23 (2016).

[24] Y. Pan, E. Yu, D. Wang, and H. Deng, Sulfur vacancy enhances the electronic and optical properties of FeS_2 as the high performance electrode material, J. Alloys Compd. **858**, 157662 (2021).

[25] S. Yang, Y. Wang, H. Zhang, Y. Zhang, L. Liu, L. Fang, X. Yang, X. Gu, and Y. Wang, Unique three-dimensional Mo_2C@MoS_2 heterojunction nanostructure with S vacancies as outstanding all-pH range electrocatalyst for hydrogen evolution, J. Catal. **371**, 20 (2019).

[26] A. Kumari, P. Ninawe, and J. M. Velázquez, Tailoring MoS_2 for small-molecule electroreduction: The role of metal doping and heterostructures, ACS Nanosci. **5**, 442 (2025).

[27] A. Mukherjee, M. Abdinejad, S. Sinha Mahapatra, and B. C. Ruidas, Controlled synthesis of copper sulfide-based catalysts for electrochemical reduction of CO_2 to formic acid and beyond: A review, Energy Adv. **3**, 2704 (2024).

[28] E. Cui, W. Zhang, X. Zhou, L. Lv, W. Chen, L. Zhou, and L. Mai, Cu_2S nanoparticle-modified copper hydroxide nanowire arrays for optimized electrochemical CO_2 reduction selectivity, ACS Appl. Nano Mater. **6**, 9361 (2023).

[29] M. Asadi, Bijandra Kumar, Amirhossein Behranginia, Brian A. Rosen, Artem Baskin, Nikita Repnin, Davide Pisasale, Patrick Phillips, Wei Zhu, Richard Haasch, Robert F. Klie, Petr Král, Jeremiah Abiade, and Amin Salehi-Khojin, Robust carbon dioxide reduction on molybdenum disulphide edges, Nat. Commun. **5**, 4470 (2014).

[30] E. J. Miller, K. P. Robinson, E. Lara, A. Berzansky, A. Baac, J. M. Velázquez, and L. Whittaker-Brooks, Atomically engineered active sites in metal trichalcogenides via dual sublattice modulation for electrocatalysis applications, ACS Appl. Nano Mater. **8**, 15869 (2025).

[31] J.-C. Yan, F.-M. Wang, S. Yin, J. Zhang, W. Jiang, and G.-G. Liu, Copper/metal oxide heterostructures for electrochemical carbon dioxide reduction, Rare Met. **44**, 2239 (2025).

[32] F. Chang, M. Xiao, R. Miao, Y. Liu, M. Ren, Z. Jia, D. Han, Y. Yuan, Z. Bai, and L. Yang, Copper-based catalysts for electrochemical carbon dioxide reduction to multicarbon products, Electrochem. Energy Rev. **5**, 4 (2022).

[33] J. Parsons and M. Alotaibi, The application of transition metal sulfide nanomaterials and their composite nanomaterials in the electrocatalytic reduction of CO_2: A review, Appl. Sci. **13**, 3023 (2023).

[34] J. Kundu, B. R. Anne, J. Cho, H. Huang, D. Cho, and S. Choi, Heterostructure engineering in metal sulfides for electrochemical CO_2 reduction: Advancing performance and stability, Small **21**, e05185 (2025).

[35] T. Shinagawa, G. O. Larrazábal, A. J. Martín, F. Krumeich, and J. Pérez-Ramírez, Sulfur-modified copper catalysts for the electrochemical reduction of carbon dioxide to formate, ACS Catal. **8**, 837 (2018).

[36] Y. Li, J. Xu, X. Luo, F. Wang, Z. Dong, K.-J. Huang, C. Hu, M. Hou, and R. Cai, Novel hollow MoS_2@C@Cu_2S heterostructures for high zinc storage performance, Nanoscale **16**, 657 (2024).

[37] X. Wang, J. Wang, X. Zhang, Q. Tian, M. Liu, N. Cai, Y. Xue, W. Chen, W. Li, and F. Yu, Nitrogen-doped Cu_2S/MoS_2 heterojunction nanorod arrays on copper foam for efficient hydrogen evolution reaction, ChemCatChem **11**, 1354 (2019).

[38] W. Zhao, J. Cao, J. Liao, Y. Liu, X. Zeng, J. Shen, X. Hong, Y. Guo, H. Zeng, and Y. Liu, Insights into photocatalytic mechanism over a novel Cu_2 WS_4/MoS_2 *S*-scheme heterojunction, Rare Met. **43**, 3118 (2024).

[39] Sk. Khaja Hussain, B. N. Vamsi Krishna, G. Nagaraju, S. Chandra Sekhar, D. Narsimulu, and J. S. Yu, Porous Co-MoS_2@Cu_2MoS_4 three-dimensional nanoflowers via *in situ* sulfurization of Cu_2O nanospheres for electrochemical hybrid capacitors, Chem. Eng. J. **403**, 126319 (2021).

[40] W. Chen, Hangtian Zhu, Qingqing Gao, Jun Luo, Yu Wang, Shuo Zhang, Ke Zhang, Chengming Wang, Yujie Xiong, Yanfei Wu, Xusheng Zheng, Wangsheng Chu, Li Song, and Ziyu Wu, Solvothermal synthesis of ternary Cu_2 MoS_4 nanosheets: Structural characterization at the atomic level, Small **10**, 4637 (2014).

[41] P. D. Tran, Mai Nguyen, Stevin S. Pramana, Anirban Bhattacharjee, Sing Yang Chiam, Jennifer Fize, Martin J. Field, Vincent Artero, Lydia H. Wong, Joachim Loo, and James Barber, Copper molybdenum sulfide: A new efficient electrocatalyst for hydrogen production from water, Energy Environ. Sci. **5**, 8912 (2012).

[42] R. H. Xu, P. P. Ma, G. F. Liu, Y. Qiao, R. Y. Hu, L. Y. Liu, M. Demir, and G. H. Jiang, Dual-phase coexistence design and advanced electrochemical performance of Cu_2MoS_4 electrode materials for supercapacitor application, Energy Fuels **37**, 6158 (2023).

[43] J. Zhou, G. Xu, Z. Zhang, and H. Wang, Facile synthesis of Cu_2MoS_4 nanosheet/multi-walled carbon nanotube composites as a high-efficiency electrocatalyst for hydrogen evolution, New J. Chem. **43**, 9574 (2019).

[44] B. Zhao, X. Qiu, Y. Song, S. Li, K. Zhang, Z. Mou, Q. Wang, B. Zhang, and Z. Wang, Regulating asymmetric charge distribution in Cu_2MoS_4 nanosheets for enhanced photocatalytic CO_2 reduction, Small **21**, 2500877 (2025).

[45] A. Ejaz, J. H. Han, and R. Dahiya, Influence of solvent molecular geometry on the growth of nanostructures, J. Colloid Interface Sci. **570**, 322 (2020).

[46] S. Bahramzadeh, H. Abdizadeh, and M. R. Golobostanfard, Controlling the morphology and properties of solvothermal synthesized Cu_2ZnSnS_4 nanoparticles by solvent type, J. Alloys Compd. **642**, 124 (2015).

[47] I. Ali, Z. Ullah, I. Rehan, A. Khalil, M. Habib, H. T. Masood, Y. Sohail, and M. Waseem, Annealing disintegrates Cu_2MoS_4 nanosheets into MoS_2 and Cu_2S nanoheterostructures, J. Mater. Sci. Mater. Electron. **28**, 15936 (2017).

[48] L. T. Le, T. T. T. Nguyen, T. T. T. Nguyen, M. T. T. Nguyen, T. T. D. Ung, and P. D. Tran, Investigation on the growth mechanism of Cu_2MoS_4 nanotube, nanoplate and its use as a catalyst for hydrogen evolution in water, Chem.: Asian J. **15**, 1873 (2020).

[49] C. F. Holder and R. E. Schaak, Tutorial on powder x-ray diffraction for characterizing nanoscale materials, ACS Nano **13**, 7359 (2019).

[50] H. Tianou, W. Wang, X. Yang, Z. Cao, Q. Kuang, Z. Wang, Z. Shan, M. Jin, and Y. Yin, Inflating hollow nanocrystals through a repeated Kirkendall cavitation process, Nat. Commun. **8**, 1261 (2017).

[51] J. Azevedo, M. P. Fernández-García, C. Magén, A. Mendes, J. P. Araújo, and C. T. Sousa, Double-walled iron oxide nanotubes via selective chemical etching and Kirkendall process, Sci. Rep. **9**, 11994 (2019).

[52] L. Zhang, A. Xu, X. Shi, H. Zhang, Z. Wang, S. Shen, J. Zhang, and W. Zhong, Electron transfer at the heterojunction interface of CoP/MoS_2 for efficient electrocatalytic hydrogen evolution reaction, RSC Adv. **14**, 19294 (2024).

[53] G. F. Harrington and J. Santiso, Back-to-basics tutorial: X-ray diffraction of thin films, J. Electroceramics **47**, 141 (2021).

[54] J. Kim, M. Ike, and K. Tokuda, Controlling the orientation of MoS_2 films on Mo metal thin film through sulfur flux regulation: A novel reaction-diffusion model, Nanomaterials **15**, 1783 (2025).

[55] F. Han, W. Li, D. Li, and A. Lu, *In situ* electrochemical generation of mesostructured Cu_2S/C composite for enhanced lithium storage: Mechanism and material properties, ChemElectroChem **1**, 733 (2014).

[56] Y. Cao, C. Zhuang, B. Wang, J. Wang, S. Chen, Q. Zhang, W. Ye, and H. Jing, Photoelectrothermocatalytic reduction of CO_2 to glycol via Cu_2S/MoS_2-Vs octahedral heterostructure with synergistic mechanism, J. Colloid Interface Sci. **666**, 141 (2024).

[57] Y. Liu, S. Jiang, S. Li, L. Zhou, Z. Li, J. Li, and M. Shao, Interface engineering of $(Ni, Fe)S_2$@MoS_2 heterostructures for synergetic electrochemical water splitting, Appl. Catal. B **247**, 107 (2019).

[58] G. Kresse and J. Furthmüller, Efficient iterative schemes for *ab initio* total-energy calculations using a plane-wave basis set, Phys. Rev. B **54**, 11169 (1996).

[59] J. P. Perdew, K. Burke, and M. Ernzerhof, Generalized gradient approximation made simple, Phys. Rev. Lett. **77**, 3865 (1996).

[60] S. P. Ong, W. D. Richards, A. Jain, G. Hautier, M. Kocher, S. Cholia, D. Gunter, V. L. Chevrier, K. A. Persson, and G. Ceder, PYTHON Materials Genomics (pymatgen): A robust, open-source PYTHON library for materials analysis, Comput. Mater. Sci. **68**, 314 (2013).

[61] D. Zagorac, H. Müller, S. Ruehl, J. Zagorac, and S. Rehme, Recent developments in the Inorganic Crystal Structure Database: Theoretical crystal structure data and related features, J. Appl. Crystallogr. **52**, 918 (2019).

[62] J. Heyd, G. E. Scuseria, and M. Ernzerhof, Hybrid functionals based on a screened Coulomb potential, J. Chem. Phys. **118**, 8207 (2003).

[63] J. Neugebauer and M. Scheffler, Adsorbate-substrate and adsorbate-adsorbate interactions of Na and K adlayers on Al(111), Phys. Rev. B **46**, 16067 (1992).

[64] J. Liu, S. Zhang, Y. A, Z. Li, X. Zhang, Y. Zhang, C. Guo, Z. Zhang, and M. Du, Interfacial electronic engineering of the 2D/2D Cu-$MoS_2/Cu_3(HIB)_2$ heterojunction for bifunctional ammonia electrolysis: Synergistic hydrogen production and wastewater detoxification, Adv. Funct. Mater. **36**, e14112 (2025).

[65] M. Hanušová, Luka Pirker, Martin Vondráček, Václav Valeš, Casey K. Cheung, Noel Natera Cordero, Amy Carl, Viktor Zólyomi, János Koltai, Ilias Sotiriou, Jens Zscharschuch, Artur Erbe, Roman Gorbachev, Jan

Honolka, Otakar Frank, and Matěj Velický, Hybridization directionality governs the interaction strength between MoS_2 and metals, Nano Lett. **25**, 12995 (2025).

[66] W. Li, Z. Zhenyu Zhang, Wenjun Zhang, and Shouzhong Zou, MoS_2 nanosheets supported on hollow carbon spheres as efficient catalysts for electrochemical hydrogen evolution reaction, ACS omega **2**, 5087 (2025).

[67] J. Wang, Y. Cui, and D. Wang, Design of hollow nanostructures for energy storage, conversion and production, Adv. Mater. **31**, 1801993 (2019).

[68] X. Li, N. Li, Y. Gao, and L. Ge, Design and applications of hollow-structured nanomaterials for photocatalytic H_2 evolution and CO_2 reduction, Chin, J. Catal. **43**, 679 (2022).

[69] H. Chen, J. Iyer, Y. Liu, S. Krebs, F. Deng, A. Jentys, D. J. Searles, M. A. Haider, R. Khare, and J. A. Lercher, Mechanism of electrocatalytic H_2 evolution, carbonyl hydrogenation, and carbon–carbon coupling on Cu, J. Am. Chem. Soc. **146**, 13949 (2024).

[70] Y. Shi, Y. Zhou, D.-R. Yang, W.-X. Xu, C. Wang, F.-B. Wang, J.-J. Xu, X.-H. Xia, and H.-Y. Chen, Energy level engineering of MoS_2 by transition-metal doping for accelerating hydrogen evolution reaction, J. Am. Chem. Soc. **139**, 15479 (2017).

[71] M. Zeng and Y. Li, Recent advances in heterogeneous electrocatalysts for the hydrogen evolution reaction, J. Mater. Chem. A **3**, 14942 (2015).

[72] H. Xu, Y. Zhang, F. Liu, Z. Yang, J. Xu, and J. Liu, Cu_2S/MoS_2 nanospheres on conductive molecule modified reduced graphene oxide for supercapacitors, ACS Appl. Nano Mater. **7**, 21340 (2024).

[73] H. Wang, X. Xu, and A. Neville, Facile synthesis of vacancy-induced $2H$-MoS_2 nanosheets and defect investigation for supercapacitor application, RSC Adv. **11**, 26273 (2021).

[74] J. C. Ortiz-Rodríguez, J. T. Perryman, and J. M. Velázquez, Charge transport dynamics in microwave synthesized one-dimensional molybdenum chalcogenides, Ind. Eng. Chem. Res. **60**, 16153 (2021).

[75] H. Vrubel, T. Moehl, M. Grätzel, and X. Hu, Revealing and accelerating slow electron transport in amorphous molybdenum sulphide particles for hydrogen evolution reaction, Chem. Commun. **49**, 8985 (2013).

[76] B.-A. Mei, J. Lau, T. Lin, S. H. Tolbert, B. S. Dunn, and L. Pilon, Physical interpretations of electrochemical impedance spectroscopy of redox active electrodes for electrical energy storage, J. Phys. Chem. C **122**, 24499 (2018).

[77] Y. Ouyang, Y. Zhang, P. S. Rice, L. Shi, J. Wang, and P. Hu, Electrochemical CO_2 reduction: Water/catalyst interface versus polymer/catalyst interface, J. Mater. Chem. A **9**, 17474 (2021).

[78] K. G. Mason, Natalia Mosqueda, S. Avery Vigil, Paola N. Del Pozo-Gonzalez, Saxton Feiner, Kingston P. Robinson, Jenna M. Ynzunza, Ankita Kumari, Rose E. Smiley, Erika La Plante, George Agbeworvi, Ivan A. Moreno-Hernandez, and Jesús M. Velázquez, Heterointercalation in Chevrel-phase sulfides: A model periodic solid for the investigation of chain electron transfer, J. Am. Chem. Soc. **147**, 18155 (2025).

[79] S. Dongare, *et al.*, Reactive capture and electrochemical conversion of CO_2 with ionic liquids and deep eutectic solvents, Chem. Soc. Rev. **53**, 8563 (2024).

[80] A. Hasani, M. A. Teklagne, H. H. Do, S. H. Hong, Q. Van Le, S. H. Ahn, and S. Y. Kim, Graphene-based catalysts for electrochemical carbon dioxide reduction, Carbon Energy **2**, 158 (2020).

[81] S. A. Francis, Jesus M. Velazquez, Ivonne M. Ferrer, Daniel A. Torelli, Dan Guevarra, Matthew T. McDowell, Ke Sun, Xinghao Zhou, Fadl H. Saadi, Jimmy John, Matthias H. Richter, Forrest P. Hyler, Kimberly M. Papadantonakis, Bruce S. Brunschwig, and Nathan S. Lewis, Reduction of aqueous CO_2 to 1-propanol at MoS_2 electrodes, Chem. Mater. **30**, 4902 (2018).

[82] J. T. Feaster, C. Shi, E. R. Cave, T. Hatsukade, D. N. Abram, K. P. Kuhl, C. Hahn, J. K. Nørskov, and T. F. Jaramillo, Understanding selectivity for the electrochemical reduction of carbon dioxide to formic acid and carbon monoxide on metal electrodes, ACS Catal. **7**, 4822 (2017).

[83] S. Wang, T. Kou, J. B. Varley, S. A. Akhade, S. E. Weitzner, S. E. Baker, E. B. Duoss, and Y. Li, Cu_2O/CuS nanocomposites show excellent selectivity and stability for formate generation via electrochemical reduction of carbon dioxide, ACS Mater. Lett. **3**, 100 (2021).

[84] T. Doulassiramane, N. Arumugam, A. I. Almansour, S. M. Mahalingam, and R. Padmanaban, An effective strategy for CO_2 reduction to C1 products using Cu-embedded MoS_2 electrocatalyst: DFT study, New J. Chem. **47**, 6932 (2023).

[85] G. Kresse and D. Joubert, From ultrasoft pseudopotentials to the projector augmented-wave method, Phys. Rev. B **59**, 1758 (1999).

[86] P. E. Blöchl, Projector augmented-wave method, Phys. Rev. B **50**, 17953 (1994).

[87] S. Grimme, S. Ehrlich, and L. Goerigk, Effect of the damping function in dispersion corrected density functional theory, J. Comput. Chem. **32**, 1456 (2011).

[88] S. Grimme, J. Antony, S. Ehrlich, and H. Krieg, A consistent and accurate *ab initio* parametrization of density functional dispersion correction (DFT-D) for the 94 elements H-Pu, J. Chem. Phys. **132**, 154104 (2010).

[89] K. Mathew, R. Sundararaman, K. Letchworth-Weaver, T. A. Arias, and R. G. Hennig, Implicit solvation model for density-functional study of nanocrystal surfaces and reaction pathways, J. Chem. Phys. **140**, 084106 (2014).

[90] K. Mathew, V. S. C. Kolluru, S. Mula, S. N. Steinmann, and R. G. Hennig, Implicit self-consistent electrolyte model in plane-wave density-functional theory, J. Chem. Phys. **151**, 234101 (2019).

[91] S. M. R. Islam, F. Khezeli, S. Ringe, and C. Plaisance, An implicit electrolyte model for plane wave density functional theory exhibiting nonlinear response and a nonlocal cavity definition, J. Chem. Phys. **159**, 234117 (2023).

[92] Y. Ren, X. Sun, K. Qi, and Z. Zhao, Single atom supported on MoS_2 as efficient electrocatalysts for the CO_2 reduction reaction: A DFT study, Appl. Surf. Sci. **602**, 154211 (2022).

[93] A. Hjorth Larsen, *et al.*, The atomic simulation environment—a PYTHON library for working with atoms, J. Phys.: Condens. Matter **29**, 273002 (2017).

[94] See the Supplemental Material at http://link.aps.org/supplemental/10.1103/84s6-812t. The supplemental file includes all the structural, morphological, and electrochemical analyses that support the findings of the article.